Journal of
Materials Chemistry A

Materials for energy and sustainability

Accepted Manuscript

This article can be cited before page numbers have been issued, to do this please use: L. J. Jiménez-Chavarriga, R. Sayago-Carro, U. Caudillo-Flores, I. Barba-Nieto, A. Tolosana-Moranchel, J. Rodriguez, M. Fernández-García and A. Kubacka, *J. Mater. Chem. A*, 2026, DOI: 10.1039/D5TA08707D.

ROYAL SOCIETY OF CHEMISTRY

rsc.li/materials-a

DOI: 10.1039/D5TA08707D

Cobalt-Niobium Co-doping of Indium Oxide: Structural and Adsorption/Catalytic Properties for CO_2 Valorization

*Luis José Jiménez-Chavarriga,[a] Rocío Sayago-Carro,[a] Uriel Caudillo-Flores,[b] Irene Barba-Nieto,[c] Álvaro Tolosana-Moranchel,[a] José A. Rodriguez,[c,d] Marcos Fernández-García,[*a] and Anna Kubacka[*a]*

a) *Instituto de Catálisis y Petroleoquímica, CSIC. C/Marie Curie 2, 28049-Madrid, Spain.*

b) *Centro de Nanociencias y Nanotecnología, Universidad Nacional Autónoma de México, Ensenada 22800, México.*

c) *National Synchrotron Light Source II, Brookhaven National Laboratory, Upton 11973, NY, USA.*

d) *Department of Chemistry, Stony Brook University, Stony Brook, NY, 11794, USA.*

Abstract

The co-doping of the indium oxide structure with cobalt and niobium is attempted using a microemulsion method to produce high-surface-area, mesoporous, functional materials. The co-doping leads to a major nanometric bixbyite oxide phase with both cations occupying cation positions, and affecting the size and shape of the oxide entities. For specific cobalt to niobium atomic ratios, the presence of a second surface phase is encountered. Such a surface phase corresponds to an ill-defined indium hydroxide-type phase. The coexistence of the two phases is a unique phenomenon associated with the presence of both cations, which play a decisive role in promoting the CO_2 adsorption capability of the solids, as well as the valorization of the molecule under dual heat-light excitation. The co-doping of indium oxide thus appears to be a unique way to intensify the analogous thermal (classical) catalytic process for the elimination/valorization of carbon dioxide.

Keyworks

Substitutionally disordered mixed oxides; Oxo-hydroxides; CO_2 adsorption and valorization; Photothermal catalysis

Email: MFG (mfg@icp.csic.es), AK (ak@icp.csic.es)

View Article Online
DOI: 10.1039/D5TA08707D

1 Introduction

Indium oxide (In_2O_3) appears as a key material with functional properties that enable practical applications derived from its good stability in various (mainly gaseous) environments, transparency in specific electromagnetic ranges as a thin film, and sensitivity resulting from electrical conductivity. This allows a wide range of industrial applications, including gas sensing for detecting volatile and hazardous compounds, transparent electrodes in photoelectrochemical systems, display technology, and other fields, as well as advanced thin films for electronic devices such as transistors.[1,2] It also finds application in the field of photo and photothermal catalysis, as it serves as a semiconductor that absorbs light and generates electron-hole pairs, which can interact with adsorbed surface species. Within this context, the use of indium oxide is particularly focused on the development of materials able to eliminate and convert carbon dioxide (CO_2) simultaneously, rendering valuable chemical products.[3,4]

As it occurs with many functional materials, the corresponding properties of indium oxide rely on a significant number of physico-chemical properties. For photon-related (and many of the previously mentioned) field(s), a primary property driving the physico-chemical characteristics of the solid is the nanostructure. The nanostructure provides inherently high surface area materials, which are required for any surface-related application, such as catalysis. Additionally, it may favor the presence of specific polymorphs, surface terminations, and defect-related structures with electronic effects.[5–7] Indium oxide displays, in the nanometric range, a bixbyite-type structure (space group $Ia\bar{3}$), where the packing resembles the fluorite structure with 1/4 oxygen atoms missing. Thus, a potentially interesting relaxation or facile movement of the cubic closest-packed oxygen positions can occur. The presence of ill-defined surface phases, in one way or another, related to the presence of indium hydroxyl or oxo-hydroxide phases, is also

View Article Online
DOI: 10.1039/D5TA08707D

known. In these nanostructures, oxygen-defect structures are crucial for promoting electron conductivity and thus facilitating the adsorption of surface species, while also generating surface-related electronic localized states.[8] The nanosized indium oxide usually adopts a primary particle with a spherical shape; however, In_2O_3 can also be obtained with non-spherical (rod, wire) shapes, the latter of which significantly facilitates the presence of anion-type (oxygen) punctual defects. Finally, quantum confinement and the concomitant band gap modification can be of significant importance. A blue shift is commonly observed for the band gap energy with the decrease of primary size.[5,6]

Doping is a common technology used in the case of indium oxide to enhance its functional properties. For photon-related catalytic applications, cationic species located at both surface and bulk positions have been tested. Normally, the formation of substitutional disordered mixed oxide structures, where indium is partially replaced by the doping cation, is obtained. This process exerts a significant effect on the structure due to the potentially different cationic sizes, the subsequent alteration of local order, and the presence of defects to achieve electroneutrality. The second effect is the presence of localized electronic states, which depend on the behavior of the cation as an acceptor or donor of charge. A random distribution of substitutional acceptors/donors of charge can result in a Guassian-type density of states at the upper/lower part of the valence/conduction bands. Such localized electronic states can be observed in conjunction with those related to oxygen anions or other types of punctual defects.[5,9,10] Upon light excitation, all dopand/defect-related electronic states can play a role in charge trapping and recombination.[3] An even more complex process can take place when two cationic species are used in the doping process. In many cases, donor-acceptor pairs are utilized, and the ratio between them primarily governs physico-

View Article Online
DOI: 10.1039/D5TA08707D

chemical effects. For nanosized indium oxide, we are only aware of a single work that uses co-doping with Zr as an acceptor and Sn as a donor. Compensated (ratio aiming to provide an equal number of donor/acceptor-related charge species) or non-compensated doping is usually pursued based on the physico-chemical properties required by the functionality. In the mentioned study, a Sn/Zr ratio above 1 was utilized to promote electron conductivity.[11]

In addition to the structural/electronic effects of the doping of the oxide, cations can also play an active role in catalysis. In this contribution, due to the catalytic implications, we aim to explore the use of cations with a promotional effect on the catalytic activity of indium oxide-based systems for the valorization of carbon dioxide (CO_2). The control of CO_2 presence in the atmosphere or at industrial emission points is as a technological requirement to limit the effects of global warming. Besides carbon capture, the chemical transformation of the molecule appears as one of the most researched fields. Catalysis plays a fundamental role in transforming the mentioned molecule into chemical forms of industrial interest.[12,13] Within this context, the development of dual materials capable of exhibiting catalytic properties under simultaneous excitation by light and heat has attracted attention. The achievement of synergy is required for a potentially interesting application of the dual light-heat intensified photothermal approach. Usually, such synergistic use of energy sources allows for a decrease in the temperature of classic thermal operation, limiting deactivation and extending lifetime, as well as by the catalyst, increasing quantum efficiency.[14,15]

For the valorization of CO_2, the promotion of photothermal catalytic activity in oxide-based systems using non-noble metals, such as copper and cobalt, has been explored previously.[16,17] In the case of cobalt, a combined experimental-theoretical analysis of

View Article Online
DOI: 10.1039/D5TA08707D

the doping process indicates a limit of solubility (doping limit) at the indium oxide structure of ca. 4-5 mol.% (cationic basis).[18] The limit of solubility coincides with the solid Co-In mixed oxide, which displays maximum activity.[18] As novelty, we studied the combination of cobalt with niobium here. In the mentioned reaction, niobium has been shown to trigger photothermal activity as a surface species on indium oxide; however, we are not aware of any work studying the doping process.[19] In the analyzed solids, the cobalt content is fixed at 4 mol.%, and the Co/Nb ratio is explored from ca. 0.5 to 2. The structural and electronic properties of the solids are studied, and their functional properties are screened in the interaction (adsorption) with the CO_2 molecule and its photothermal valorization. The work we will prove that a strong catalytic synergy is reached with the cooping process. The physico-chemical origin of such a functional effect is unveiled.

2. Experimental Section

2.1 Synthesis of materials

Catalysts were prepared using a procedure based on the use of inverse microemulsions. Two equal organic phase solutions of n-heptane, Triton X-100 (surfactants), and hexanol (co-surfactant) were stirred for 30 min. Then, an aqueous solution (corresponding to a water to surfactant ratio of 18:1) containing the (In, Co, Nb) precursors was added dropwise into one of them. In the second organic phase solution, tetramethylammonium hydroxide (TMH; Aldrich; 25 v/v%) was slowly incorporated. The TMH incorporated has a 3:1 molar relationship with the cation content of the first microemulsion. The precursors mentioned were indium nitrate (Aldrich), cobalt nitrate (Aldrich), and ammonium niobate (V) oxalate (Sigma-Aldrich). Cobalt is used in a 4 mol% concentration, and Niobium between 2.5 and 7.5 mol% (expressed in total cation

View Article Online
DOI: 10.1039/D5TA08707D

basis). The microemulsions were stirred for an hour and mixed, adding the TMH-containing microemulsion to the one with In, Co, and Nb precursors in order to precipitate the cations. The final solution was kept stirring overnight. Afterwards, the mixture was washed twice with ethanol, centrifuged, and dried at 80 ºC, resulting in a powder. Finally, the powder was calcined for 2 h at 350 ºC. Samples are named as InxCoyNb, where x and y correspond to the molar percentage of Co and Nb (cation basis) attempted at the synthesis stage.

2.2 Characterization of the materials

The catalysts underwent comprehensive physical and chemical characterization. First, XRD patterns were acquired employing a Bruker D8 Advance diffractometer (Germany) with Ni-filtered Cu-Kα radiation (λ = 0.15406 Å). UV-vis spectra were recorded using a Varian Cary 300 spectrophotometer (USA) to measure the band gap energy. The physisorption experiments with N_2 were conducted using a Micromeritics Tristar-II 3020 equipment (USA) to determine average pore sizes and surface areas. Then, the XPS technique was utilized using a SPECS spectrometer (UK), featuring a PHOIBOS 150 WAL hemispherical energy analyzer, an XR 50 aluminum X-ray source, and a μ-FOCUS 500 X-ray monochromator. Additionally, elemental analysis was performed using Inductively Coupled Plasma Optical Emission Spectroscopy (ICP-OES) with a Perkin Elmer Avio 220 Max (USA), enabling a comparison of the material´s composition. Photoluminiscence (PL) spectra were recorded with an excitation energy of 365 nm using a Perkin-Elmer LS-50B Luminescence Spectrometer (USA). The local rate of photon absorption was obtained using measurements with the help of a PerkinElmer Lambda 1050 UV-Vis-NIR spectrometer (USA).

Mott-Shottky plots were obtained using an Autolab PGSTAT320N potentiostat/galvanostat with an electrochemical impedance spectroscopy module

View Article Online
DOI: 10.1039/D5TA08707D

FRA32M controlled by the NOVA 2.1 software. The electrodes were prepared by coating a RDE glassy carbon electrode (5-mm diameter, Pine Instruments) with three drops of 10 µL each. The ink was prepared by mixing 2.5 mg of catalysts, 480 µL tetrahydrofuran (THF) and 30 µL of Nafion 117 solution (5%) with an Ultrasonic mixer UP50H (Hielscher). The experiments were performed in three-electrode cell, using an Ag/AgCl (3 M) electrode and a Pt wire as reference electrode and counter electrode, and the RDE electrodes as working electrodes. 0.1 M Na_2SO_4 (Aldrich, ACS reagent, >99%) solution (pH 7.3) was used as electrolyte. Mott-Schottky measurements were conducted in dark conditions, recording impedance spectra at different potentials within a frequency range from 1 Hz to 100000 Hz with 10 points per decade and a voltage amplitude of 10 mV. A Randles circuit was used to fit the spectra and to estimate the space charge layer capacitance at each potential. To estimate the flat-band potential, the values obtained at 5000 Hz were selected.

Scanning transmission electron microscopy (STEM) was performed in high-angle annular dark-field (HAADF) mode in an Cs-corrected JEOL ARM200F microscope (LUME@UNAM, RRID: SCR_024400). The equipment is equipped with an Oxford AZtecTEM silicon detector for Energy-dispersive X-ray spectroscopy (EDS).. Furthermore, TPD (temperature-programmed desorption) experiments were carried out using a Micromeritics Autochem II 2920 (USA). The procedure starts at 140 ºC for 10 min under a nitrogen flow for cleaning. After cooling, the temperature was maintained at of 50 ºC for 40 min under a mixture of CO_2 and Nitrogen (1:9; 30 mL min^{-1}). The next step is a 30-minute desorption, changing the mixture for Helium (25 mL min^{-1}). After it, the TPD experiment is carried out up to 800 ºC.

The 8-ID beamline of the NSLS-II synchrotron at Brookhaven National Laboratory (NY, USA) was utilized for XAS (X-Ray absorption fine structure) experiments.[20] They

View Article Online
DOI: 10.1039/D5TA08707D

were conducted in order to acquire data of the indium K-edge (27940 eV, metallic In), cobalt K-edge (7709 eV, metallic Co), and niobium K-edge (18986 eV, metallic Nb). XANES (X-Ray absorption near-edge structure) and EXAFS (Extended X-Ray absorption fine structure) spectra were acquired in fluorescence mode for Co and Nb and transmission mode for In. The samples were prepared by placing catalyst powders between 2 Kapton tapes, and a reference foil of each element was used for energy calibration. The beamline is equipped with X-ray optics including a Pt/Si/Rh coated collimating mirror system, a high-heat-load Si (111) monochromator for energy selection, a Pt/Rh coated focusing toroid mirror for focusing, and, in the end-station, the high harmonic rejection mirror system (Rh/Si/Pt). The policapillary lens allows a higher focusing potential. Theoretical phase and amplitude functions were calculated using FEFF for EXAFS fitting and tested with model compounds. Apart from the metallic foils, the references measured are In_2O_3, CoO, Co_3O_4, and Nb_2O_5. Both XANES and EXAFS analyses were carried out using Demeter's programs Athena and Artemis.[21] Fittings were carried out following the k^1, k^2, k^3 procedures described by the International X-ray absorption society, and the number of free parameters calculated in accordance with the Nyquist theorem.[22,23]

Diffuse reflectance infrared spectroscopy (DRIFTS) was utilized to measure the catalyst response to the reaction environment. The apparatus is a Bruker Vertex 80 FTIR spectrometer using an MCT detector and running under OPUS/IR software. After calcination of the samples in the measurement chamber (HVC, Harrick Scientific, calcination at 350 ℃ as described in section 2.1), the temperature was decreased to 250 ℃, where maximum photothermal effects were observed. The infrared experiments were carried out isothermally at 250 ℃, using a constant total flow of 10 mL min^{-1}. Initially, the samples were contacted with a 20 % CO_2/N_2 stream, and the signal was

View Article Online
DOI: 10.1039/D5TA08707D

recorded until stable behavior. After it, a purge of 5 min in pure N_2 to eliminate gas-phase CO_2 was followed by the signal recording under a 20 % H_2/N_2 stream.

2.3 Activity measurements

The indium-based catalysts were tested using a Pyrex cylinder in which the powder catalyst, dispersed in a methanol solution by sonication, was spread to create a homogeneous layer after drying. The cylinder was inserted into another tube under a coaxial configuration (see Figure S1). The gases flowed in the space between cylinders, establishing contact with the catalyst deposited on the inner tube. The gas mixture was formed by 20% CO_2, 20% H_2, and 60 % N_2 (total flow rate 10 mL min^{-1}). The tubes were placed inside a metallic box with four LED lamps (top, bottom, left, and right) symmetrically positioned around the coaxial cylinders. Inside the inner tube, a compensated heating resistor was used to test the thermal catalytic part. An Agilent GC 8890B chromatograph (USA; equipped with two TCD and one FID detectors) is used for the detection of the products, allowing the calculation of the rates and selectivity of the reaction. In this work, CO was the main reaction product, as described below. Full details about the illumination systems, heating, gas-feeding control, reactor construction, FID and TCD detection, as well as quantum efficiency, reaction rates, etc, calculated following the International Union of Pure and Applied Chemistry (IUPAC) recommendations, can be found in Supporting Information.

3. Results and discussion

3.1 Synthesis and main physico-chemical properties

As previously detailed, the microemulsion method can provide significant control over the morphological properties (primary particle size and shape, surface area, etc.) of

View Article Online
DOI: 10.1039/D5TA08707D

nanostructured solids. It is also a particularly suitable method for doping oxide structures with significant structural homogeneity, leading to highly dispersed doping species.[24] As will be shown in this section, this is the case for the Co, Nb co-doping samples synthesized here. We tested solids with a 4 mol% of Co and Nb in the range of 2.5 to 7.5 mol. %. The chemical analysis of these powders indicates that Co and Nb are present in the nominal concentrations with an error of 4.6 % (Table S1). The calcined solids were examined using TEM. Bright and dark field HR-TEM images of the In4Co5Nb sample, and In4Co and In5Nb reference samples are presented in Figure 1. Figure S2 contains micrographs for the In4Co2.5Nb and In4Co7.5Nb samples. The presence of nano-entities with sizes of around 10 nm or below can be observed in all cases. The nanocrystalline particles lead to a highly porous structure in all cases, as detailed below. The single-doped Co-containing sample exhibits particles with pronounced anisotropy, displaying a (small rod) batonnet-type morphology (Fig. 1a-c). As the most abundant surface termination, we detected the (222) planes with a ca. 2.91 Å periodicity of the cubic bixbyite-type In_2O_3 oxide polymorph (space group $Ia\bar{3}$).[7] In the case of the In5Nb reference, the morphology of the primary particle is different (Fig. 1i-j). Rounded-shaped particles co-exist with batonnet-type particles, which results in the presence of additional surface planes, such as the (400) one of the bixbyite-type structure. The co-existence of Co and Nb doping species leads to a more complex case (Fig. 1d-f), where non-isotropic batonnet-type particles disappear gradually up to 5 mol. % of Nb, with minimal presence for the In4Co7.5Nb solid. Figure S3 provides further visual proof of the change of morphology from the (batonnet-type) small roads typical of In4Co to the rounded-shape morphology predominant in the In4Co7.5Nb case. A detailed view of these non-isotropic particles (Fig. 1g-h) reveals perfect crystallographic order within the particle, with no signal of isolated point defects. The nanoparticles

View Article Online
DOI: 10.1039/D5TA08707D

display a size of approximately. 4-5 x 8-10 nm and a (222) surface termination, resembling the single-doped Co reference sample. In parallel to the shape modification, the average size seems to grow moderately compared to the single-doped Co reference samples.

Further information can be obtained by analyzing the textural and structural properties of the solids. In Fig. 2 (panels a, and b), we present the nitrogen adsorption-desorption isotherms. The profiles are, in all cases, characteristic of mesoporous materials, displaying a typical H4 type loop dominated by adsorbate-solid interactions.[25] A difference is observed in the initial p/p^o value, where the plateau is detected after the hysteresis loop in the co-doped samples. Table 1 collects quantitative parameters to appraise such differences. Firstly, BET surface area values indicate that the single-doping process reduces the area obtained for the pure indium oxide reference sample prepared using the same method. The co-doping process further promotes the decrease in surface area. A similar qualitative behavior is observed with the average pore size parameter. However, the In4Co2.5Nb sample displays the lowest value, in accordance with the different isotherm profile. The behavior of the BET surface area is closely linked to the changes observed in the primary particle size and shape, as measured using microscopy. Fig. 2c encloses the XRD patterns of the samples, while Fig. 2d-f show zooms of selected regions. The patterns are dominated by the cubic bixbyite-type In_2O_3 oxide structure (space group $Ia\bar{3}$),[7] in accordance with the microscopy study. The (211), (220), (400), very broad (411), (332), and (431), as well as the (440), (611), and (622) diffracting peaks are detected at 21.09, 30.27, 35.31, 37.33, 41.57, 45.54, 50.82, 55.87, and 60.35 degrees, respectively. Table 1 collects the bixbyite primary particle size obtained from XRD measurement. The doping of the indium oxide always triggers an increase in the particle size, which is modest for Nb than for Co. The presence of both

View Article Online
DOI: 10.1039/D5TA08707D

cations seems a complex case. Despite this, as mentioned above, a rough inverse correlation can be detected between the primary particle size and the BET surface area. This may indicate that the loss of surface area triggered by the doping process is, at least in a major part, connected with the observed change in primary particle size and shape.

The zoom views presented for the XRD patterns (Fig. 2d-f) provide evidence of the presence of a second phase. Vertical dotted-dashed lines mark the main diffraction peaks associated with this phase. To provide a conclusive assignment for this phase, we carried out a temperature-dependent XRD study of the calcination step. Relevant results are presented in Fig. S4 and S5. As shown earlier by the outstanding work of Nielsen and coworkers,[7] the wet-preparation methods usually generate the formation of the $In(OH)_3$ phase (space group $Im\bar{3}$). This distorted ReO_3-type phase is stable up to ca. 200 ℃ in air. Figures S4 and S5 demonstrate the presence of this phase in all samples treated at this temperature. This phase evolves into the cubic bixbyite indium oxide structure at ca. 300 ℃. In our case, the phase transition at 300 ℃ is illustrated with the presence of broad peaks ascribable to one or two ill-defined phases, depending on the sample. At 350 ℃, this phase transformation is complete, rendering nanostructured (bixbyite-type) indium oxide and the single-doped powders. However, for the samples In4Co2.5Nb and In4Co5Nb, we observed additional peaks (in addition to the bixbyite ones) that are related to the initial $In(OH)_3$-type phase. These peaks are, in most cases, rather broad and are marked with an asterisk in Figures S4 and S5. It seems that a significant number of the original (pattern(s) at 200 ℃) $In(OH)_3$ peaks are not observed in the calcined materials, indicating some restricted growth that may be interpreted as an effect of the major bixbyite phase and may indicate an epitaxial growth. This is further discussed with the help of XAS. In addition, the $In(OH)_3$–related peaks appeared at lower distances, showing a significant decrease of ca. 0.2 Å of the cubic cell parameter (from

View Article Online
DOI: 10.1039/D5TA08707D

that of the $In(OH)_3$ treated at 200 ℃; 7.95 Å) for both samples, In4Co2.5Nb and In4Co5Nb. Finally, we note that the maximum content of Nb (In4Co7.5Nb) does not allow the presence of such a phase, as occurs with the single-doped samples. The existence of the (epitaxial) hydroxide-related phase could be connected with the change in size/shape of the primary particle triggered by the co-doping process. The appearance of new surface terminations (e.g., likely related to the change of shape) as a function of the Co/Nb ratio (Fig. 1) would only stabilize the mentioned phase for sizes below 10 nm (Table 1).

To complete the analysis of the main physico-chemical properties of the solids, Figure S6 collects data from UV-visible, electrochemical, and photoluminescence spectroscopies. UV-visible profiles are characteristic of the semiconductor nature of the powders, with a marked decrease of absorbance at the band gap energies (Fig. S6a). Band gap values, considering that indium oxide is an indirect-gap semiconductor, are collected in Table 1.[5] The doping with Co increases the band gap energy. As theoretical analyses showed, this may be due to the stabilization of Co^{2+} states, which suppresses the spin in the dopand cation and affects the conduction band edge states.[18] Although the effect of Co^{3+} is not known, we note that the Co^{2+} oxidation state contributes significantly to the Co oxidation state distribution of the In4Co sample according to the XANES results (see below). The Nb doping affects the band gap energy of the bare indium oxide reference to a lesser extent. On the contrary, the co-doped samples exhibit an increase in the band gap energy value compared to the bare oxide, a behavior reminiscent of the single-doped Co case (Table 1). There is no noticeable effect of the ill-defined $In(OH)_3$-type phase on the UV-visible spectra, as this phase shows a band gap energy of ca. 5.1 eV.[26] This may be related to the limited contribution (molar content) of such a phase, as will be shown using XAS. The presence of anion-related

View Article Online
DOI: 10.1039/D5TA08707D

defects may be envisaged in the indium oxide. According to TEM, they can be present at the steps and edges of the particles, as very few defects are observed in the main surface planes.[18] To further evaluate the effect of the doping on the In_2O_3 bixbyite-type band structure, the flat-band potentials (E_{FB}) were estimated from Mott-Schottky plots (Figure S6b). The extrapolation of the linear trend in the Mott–Schottky plot to the x-axis (potential) gives the value of the flat-band potential. The In_2O_3 doped catalysts with only Co or Nb showed values of the E_{FB} close to -0.4 and -0.03 V vs RHE, respectively. On the other hand, In_2O_3 and In_2O_3 doped with both Co (4%) and different amounts of Nb (2.5-7.5%) led to values of the E_{FB} between those found for In4Co and In5Nb materials (around -0.19 - -0.25 V vs RHE). The positive slope of the fittings in the plot for all the photocatalysts was positive, suggesting that they are n-type semiconductors.[27] Using these data, together with the band gap energies presented in Table 1, the conduction and valence band-edge positions for the samples were calculated and presented in Figure S6c. As can be observed, single (Co, Nb) doping affects the flat band-edge energies and the co-doped samples show rather similar band structure.

The photoluminescence experiments confirm the existence of defects as the charge annihilation process (taking place after light absorption) in nanometric oxides having an indirect-type gap usually involves the presence of localized, defect-related states.[28] Two bands at ca. 425 and 525 nm are observed after excitation with UV light of the indium oxide reference samples (Fig. S6d). The single-doping process drastically decreases the intensity of the latter band and, in the case of the co-doping, of the overall intensity, except when Nb is at the lowest content essayed (In4Co2.5Nb). A key point is that the intensity is always lower than that of the bare indium oxide reference (Fig. S6d), indicating that doping always favors the control of charge recombination. The physical origin of the intensity is unclear, but a correlation with the flat valence band band-edge

View Article Online
DOI: 10.1039/D5TA08707D

position of single and co-doped samples (and, in turn, with the nature of the electronic states with participation of the doping or doping-anion related states) can be noticed. Independent of the physical origin, the intensity decrease of the photoluminescence signal can be considered a positive effect on photo-related catalytic processes.[3]

3.2. In, Co and Nb species: structural properties

A survey analysis of the doping cation presence in the samples was carried out using EDS. Fig. 3 contains data for the In4Co2.5Nb and In4Co7.5Nb samples. Results for the single-doped reference samples and the In4Co5Nb sample are presented in Fig. S7-S9. In all cases, the Co and Nb species seem to be present in the samples with high dispersion. The absence of agglomerates containing Co or Nb as a single component can be noticed, in accordance with the results presented in the previous section. Further information is obtained with the help of XPS and XAS spectroscopies.

The In 3d XPS spectra of the samples are presented in Fig. 4a. An essentially invariant binding energy is detected for all samples. The 444.1 eV binding energy observed for the $3d_{5/2}$ peak is ascribable to an In(III) oxidation state.[29] The similarity of the local environment of indium in all the samples under study is confirmed by the XANES spectra (Fig. 4b). XANES shows an invariant adsorption edge at ca. 27938.0 eV and a complete lack of differences in the electronic properties of the In species present in the catalytic solids with respect to the bare oxide reference sample.[30] The Fourier transform of the EXAFS spectra further corroborates the essentially identical local order (local environment) observed around the In centers, irrespective of the absence or presence of doping cations (Fig. 4c). Considering that the In4Co2.5Nb and In4Co5Nb samples contain a distorted $In(OH)_3$–type phase (Fig. 2), the XAS study strongly suggests that it corresponds to a minor phase, not visible by both XANES and EXAFS. This indicates a limited contribution (below 10 mol%). As suggested previously, some kind of intense

View Article Online
DOI: 10.1039/D5TA08707D

interaction between the mentioned hydroxide-type phase over the major bixbyite In_2O_3 would be present in the In4Co2.5Nb and In4Co5Nb samples. This may lead to epitaxial growth, which could explain the strongly distorted structure (as indicated by XRD results) and the absence of any XAS signal for the minor phase, the latter being triggered by a combined effect of disorder and low content.

Cobalt appears to be a more complex case from a structural/electronic point of view. The Co XPS signal display essentially the same intensity for all samples. The Co/In atomic ratio measured with XPS is 40 % higher than the one obtained by chemical analysis. As the single-doped case showed the presence of cobalt at near-surface positions,[17] this also appears to be the case for the co-doped samples. Considering the XPS signal, the Co $2p_{3/2}$ signal peaks at ca. 780.4 eV in all single and co-doped solids (Fig. 5a). This binding energy points out the existence of Co(II) type species.[31] The presence of such oxidation state in Co-doped samples appears in accordance with the theoretical analysis presented in the literature.[18] Nevertheless, the XANES profile of the samples displays evident differences with the CoO (as other Co oxides) references (Fig. 5b). On the contrary, the absence of significant differences can be observed between single and co-doped samples. The higher intensity of the white line (exemplified by the intensity value at ca. 7724.0 eV) with respect to the CoO and Co_2O_3 oxide references points out the increased degree of the covalent character of the Co(3d)−O(2p) interaction in the initial state of the samples with respect to the mentioned oxide references. This fact is characteristic of sub-nanometric and/or isolated Co(II) type species.[32] To further analyze the cobalt oxidation state in the doped samples, the broadly applied integral method was utilized.[33] This leads to an average Co oxidation state of ca. 2.45, relatively close to the Co(II) previously mentioned. The significant differences with the cobalt oxide references are also visible in the Fourier transform of the EXAFS

View Article Online
DOI: 10.1039/D5TA08707D

spectra (Fig. 5c). Neither the Co-O first shell nor the higher order shells appear to have a clear correspondence with those describing the local order of CoO or Co_3O_4. The local order details will be unveiled below by fitting.

The study of the niobium species presented a simpler case than that of cobalt. The Nb 3d XPS signal is presented in Fig. 6a. The $3d_{5/2}$ peak shows an invariant binding energy value of 206.6 eV. This value indicates the presence of Nb(V) species in an oxidizing environment.[31] The XANES spectra of the samples also lack differences among the solids under study (Fig. 6b). Some minor differences with the bare niobium oxide reference. They correspond to the lower intensity of the pre-edge at ca. 18993.0 eV as well as the slightly higher d-splitting of the white line. Both facts would indicate a local environment different from the reference, as may be expected from the relatively low symmetry (from a pentagonal bipyramid or a strongly distorted octahedral) of the Nb(V) single oxide(s) to the more symmetric octahedral-type structure typical of indium oxide.[34,35] The Fourier transform of the EXAFS spectra shows a relatively similar profile for single and co-doped samples, but with significant differences with the niobium oxide reference (Fig. 6c). As happens with cobalt, differences in the Nb-O and further shells become evident with respect to the bare reference oxide.

For the cases of cobalt and niobium species, we thus carried out the fitting of the EXAFS spectra to further analyze the structural details of the local order around the doping cations. The outcome of this procedure is summarized in Table 2 for the cobalt case and in Table 3 for the niobium case. The goodness of the fitting can be observed in Fig. 7. According to the Nyquist theorem, a minimum of 14 free parameters can be used in the fitting in the case of Cobalt. In Table 2, this allows the use of four different coordination shells. As expected from the XPS-XANES analysis, the Co-O first shell shows a coordination number close to 6. After that shell, two main Co-In contributions

View Article Online
DOI: 10.1039/D5TA08707D

are observed at distances of ca. 3.30 and 3.80 Å. The distances resemble the cation-cation distances of the indium oxide, with a shortening due to the smaller ionic radius of the doping cation.[7,36] The analysis of these three coordination shells provides an unequivocal proof that cobalt is substituting indium in the bixbyite structure, forming a substitutionally disordered mixed oxide. A fourth shell is detected, indicating the presence of a Co-Co contribution at ca. 3.20 Å (Table 2). This can be envisaged as a partial substitution of indium by cobalt in the first cation-cation distance. The strong decrease with respect of the Co-In distance could be rationalized considering the (cobalt) lower ionic radius but also the presence at near surface positions, as suggested by XPS, which may allow a larger freedom to accommodate the differences in distances. In the case of niobium, the fitting only requires three shells (Table 3). The Nb-O contribution appears at two coordination distances, resembling the pure niobium oxide environment. The distances are, however, larger than those of the bare niobium oxide, indicating again the presence of the doping cation in the bixbyite structure (Table 3). The important differences in ionic size of Nb(IV) with respect to In(III) and/or in local electrostatic forces can rationalize this point.[37] A Nb-In coordination shell corroborated the doping process. This shell owns a characteristic distance of indium oxide. A difference with cobalt can be however noticed. The Nb/In XPS ratio goes from $0.7x10^{-2}$, $1.3x10^{-2}$, and $1.9x10^{-2}$ for the In4Co2.5Nb, In4Co5Nb, and In4Co7.5Nb solids, respectively. They are all well below the corresponding ratios measured by chemical analysis (Table S1), indicating the preferential position of niobium in the bulk of the materials. Finally, it can be noted that the coordination number of the Nb-In shell decreases from 6 to 4.6 for the In4Co7.5Nb sample. This would result from an increasing disorder of the structure.

View Article Online
DOI: 10.1039/D5TA08707D

In summary, we would thus see that the co-doping process yields a substitutionally disordered bixbyite-type oxide structure, with cobalt and niobium occupying cationic positions. Cobalt is present at surface and near-surface positions, while niobium is primarily located at bulk positions. The surface cobalt may facilitate the activation of the carbon dioxide molecule. However, its unique electronic properties (cobalt presents a +2.5-oxidation state) would make it difficult to interpret the exact role of cobalt. A more critical result could be the presence of an additional (minor, below 10 mol. %) indium-containing phase for specific Co/Nb atomic ratios (4/2.5 to 4/5; samples In4Co2.5Nb and In4Co5Nb, respectively). An epitaxial, strongly distorted $In(OH)_3$-type phase is detected. The XAS study indicates that although the co-presence of cobalt and niobium is required to generate this phase, they are not doping such a polymorph. According to the band positions of the oxide and hydroxide indium-containing phases,[38] their contact will trigger an effective charge separation after light excitation. This would contribute to the decrease of intensity observed for the photoluminescence signal in co-doped samples (Fig. S6d).

3.3 Functional properties

We started the analysis of the functional properties by studying the interaction of CO_2 with solids using TPD. The temperature of desorption of a molecule from the surface of a solid is proportional to the strength of the molecule-solid interaction. It is typically analyzed in terms of the low (below 100 ℃), medium (up to ca. 300-350 ℃), and high adsorption strength of the interaction.[39,40] The fitting of the TPD profiles of the co-doped samples is presented in Fig. 8a-c. TPD results for the single-doped reference solids are shown in Fig. S10. All samples show desorption of adsorbed molecules from ca. 50 to around 800 ℃. Above approximately 350 ℃, the desorption of carbonate-type species occurs, with little relationship to the catalytic activity for the valorization of

View Article Online
DOI: 10.1039/D5TA08707D

CO_2 using water or hydrogen.[41] In this context, we would pay particular attention to the medium-strength molecules, as they are directly connected with the photothermal catalytic properties described below.

In any case, the total amount of adsorbed CO_2 normalized per gram of solid is plotted in Fig. 8d and 8e with respect to the amount of cobalt or niobium metal or the BET surface area of the solids, respectively. Speaking about the single-doped materials, it is clear that cobalt positively influences the adsorption of the molecule with respect to niobium. This could be an effect of the near-surface position of the cobalt. Although there are differences between co-doped solids, they are roughly equal within error, and they do not differ strongly from the result of the In4Co reference. So, in terms of total adsorption of carbon dioxide, the co-doping process appears to provide a somewhat similar behavior to the In4Co reference. Interestingly, the medium-strength desorption presents a completely different behavior (Fig. 8f). It displays a behavior dominated by the BET area, but shows an inverse correlation. Importantly, the In4Co2.5Nb and In4Co5Nb promote the medium-strength absorption of the CO_2 molecule. The physical cause of this behavior appears to be connected with the surface presence of the ill-defined, strongly distorted $In(OH)_3$-type phase. This phase alters the interaction of the molecule with the surface, creating new adsorption centers and promoting, as mentioned, the medium-strength fraction.

The catalytic properties of the solid were tested in the valorization of CO_2 under dual excitation, utilizing both light and heat as energy sources. CO was obtained as the main product together with traces of methane. The minute quantities of methane would indicate the limited hydrogenation capability of the catalysts. High selectivity to CO, always above 98.2 %, was observed for all samples. In particular, the co-doped samples produce CO almost selectively, independently of the H_2:CO_2 ratio employed (see Table

View Article Online
DOI: 10.1039/D5TA08707D

S2). Thus, through the reverse water-gas shift reaction, our co-doped catalysis yielded almost exclusively carbon monoxide, a common outcome under photothermal conditions for indium-based catalysts.[17,42–44] Fig. 9 collects these results, showing the activity of the solids under thermal and photothermal catalytic conditions, using various reaction temperatures ranging from room temperature to 350 ℃. Negligible activity is observed from temperatures below 200 ℃. A boost in activity is observed from 250 ℃, except for the In5Nb reference sample, which shows a similar boost around 300 ℃. The behavior of the co-doped samples exhibits differences between the highest loading (In4Co7.5Nb) and the other solids (In4Co2.5Nb and In4Co5Nb), which again seems to be connected with the absence or the presence of the ill-defined, strongly distorted $In(OH)_3$-type phase. In addition, Fig. 9 (bottom panel) also shows the synergistic results for the use of the two energy sources (measured using equation S1). The excess function is positive between 200 and 300 ℃ for the In4Co2.5Nb and In4Co5Nb. It reaches ca. 50 % at 250 ℃ and ca. 25 % at 300 ℃ for the In4Co5Nb solid. Thus, this last sample renders the optimum of the synergy function. Note that the synergy is observed for different H_2:CO_2 ratios (Table S2). The high excess rate values presented show that the co-doped solid is a material that can allow the intensification of the classic thermal process. It is also interesting to note that the optimum photothermal effect is achieved through the effective use of light. The quantum efficiency value (calculated using equation S2) for the In4Co5Nb sample is 7.3×10^{-2} %, 40% higher than the maximum value reported previously for co-doped indium oxide.[17] At the optimum photothermal conditions, for the mentioned In4Co5Nb sample, the quantum efficiency (calculated using equation 2, with the temperature affecting both the reaction rate and the $e^{a,s}$ parameters) increases by ca. 100 times, further confirming the synergy achieved under dual photothermal conditions. Nonetheless, the relatively low quantum efficiency would

View Article Online
DOI: 10.1039/D5TA08707D

indicate that the thermal activation of the molecule is crucial. The effects of light under photothermal conditions would thus be related to localized effects on the active site of the reaction. Finally, it is worth mentioning that the co-doped catalysts exhibit stable catalytic behavior under prolonged time-on-stream tests. This is shown here for the most active In4Co5Nb sample. Fig. S11 displays the corresponding reaction rate at 250 ℃ during three consecutive thermo-photothermo cycles for a total of 72 h. The reversible response between thermo and photothermal conditions, as well as the stable activity achieved for the whole period, can be noticed.

The existence of two indium-containing phases is, as mentioned, unique, as they cannot be obtained in the bare oxide or the single-doped materials for samples calcined in air, as is the case here. Although the promoted effect of light is a result of the presence of the strongly distorted hydroxide-type component at the surface of the bixbyite phase, this does not appear directly correlated with a specific effect on charge carrier recombination. The single and co-doped samples show a decrease in the charge recombination with respect to the bare indium oxide. However, the photoluminescence measurements (Fig. S6d) show, for example, substantial differences between the In4Co2.5Nb and In4Co5Nb samples. On the contrary, the effect on the adsorption capability of the CO_2 in the adequate range of temperatures (Fig. 8f) appears directly connected with the activity (Fig. 9). This happens despite the lower surface area of these two samples, providing convincing evidence that the generation of adequate surface centers for CO_2 (e.g., in one way or other related to the presence of the ill-defined indium hydroxide-type phase) plays a key role in thermal and photothermal conditions. Together with the optimization of charge recombination achieved from the bare indium oxide reference, they may explain the synergy in dual excitation conditions. The high activity of oxo-hydroxide indium-containing phases has been previously presented in

View Article Online
DOI: 10.1039/D5TA08707D

photo and photothermal CO_2 valorization reactions. The profit of light in dual light-temperature reaction conditions is achieved through internal charge handling due to a gradient of oxygen deficiency as a function of the distance from the surface of the material.[45,46] Here, we achieve a somewhat different positive result, as although charge recombination and handling are always favored in single and co-doped materials, the differential factor associated with the co-doped materials is the alteration of the interaction with and the subsequent activation of the CO_2 molecule.

To prove this conclusion, an in-situ infrared study was carried out. The contact of CO_2 at 250 ℃ with the samples generated several surface species (Figures 10a,b,c). As will be justified below by their evolution under hydrogen, we observed two chelating or bridging carboxylate species, with asymmetric COO stretching modes of ca. 1624-1630 and 1550-1570 cm^{-1}, and a symmetric one of ca. 1428-1430 and 1375-1376 cm^{-1}, respectively.[17,47] An additional H-bonded monodentate carboxylate can be assigned using the 1550-1570 and 1233-1236 cm^{-1} contributions.[47] Note that (due to the behavior under hydrogen) at the 1550-1570 cm^{-1} region, we expect the contribution of two different chemical species. As can be observed in the figure, the illumination of the samples always favors the interaction of CO_2 with the solids. Under hydrogen and depending on the sample, some of the species evolve, and others do not (Figures 10c,d,e). The chelating bridging carboxylates appeared to lack evolution for all samples. This is not a surprising result considering that the TPD study shows that a significant number of surface species are stable at 250 ℃ (Fig. 8). In the In4Co and In5Nb samples, the infrared signal lacks, in fact, any relevant evolution (consumption) of the surface adsorbed species. On the contrary, in the co-doped samples having the ill-defined hydroxide-type phase, the H-bonded carboxylate species are consumed and would be used to generate carbon monoxide (Figure 10c). Both the initial build-up and evolution

View Article Online
DOI: 10.1039/D5TA08707D

of the last species require the combined use of light and heat (e.g., it is not observed in the absence of light).

4. Conclusions

In this work, the cobalt-niobium co-doping of the bixbyite indium oxide structure is essayed using a microemulsion method. The resulting solids are mesoporous, high surface area materials. The co-doping process results in the formation of a nanosized, substitutionally disordered bixbyite oxide phase. This is the major component for all solids, which is presented as batonnet-type nanoparticles for single-doped cobalt and is observed together with rounded-shaped particles for the single-doped pure niobium solid. The co-doping samples present a mixture of these two particle shapes, with predominance of the rounded-shaped entities for niobium content above 5 mol. %. In addition to this major phase, for Co/Nb atomic ratios of 4/2-5 to 4/5, the solids display the presence of an ill-defined, surface indium hydroxide-type phase. This minor phase, likely below 10 mol. %, is apparently free of any doping cation.

The structural analysis of the co-doping process displays a relatively low interaction between cobalt and niobium. Both occupy cation positions of the bixbyite structure, but cobalt appears as a near-surface species while niobium is in the bulk of the solids. In the case of cobalt, this leads to a shrinking of the local Co-In distances with respect to the bixbyite structure. It also shows the presence of a low number of cobalt-cobalt contacts. The nearly isolated cobalt species show an average oxidation state of ca. +2.5. For the niobium case, the local structure of the bixbyite suffers a larger change in the first (oxygen) shell, likely due to the size of the doping cation as well as the strong electrostatic forces. In this case, Niobium has a +5 oxidation state.

View Article Online
DOI: 10.1039/D5TA08707D

The adsorption and catalytic properties of In_2O_3, for CO_2 valorization, seem affected by the presence of the ill-defined hydroxide-type minor phase. This phase could be stabilized due to doping-triggered morphology effects. The presence of such phase reorders the adsorption sites for the adsorption of the molecule, favoring the medium-strength fraction, and facilitates the production and transformation of H-bonded carboxylate species, promoting activity. Thus, this surface phase appears to be key for achieving optimal photothermal catalytic properties in the valorization of CO_2 through the reverse water-gas shift reaction. The valorization is obtained with a strong synergy between light and heat, exceeding the sum of the individual-source processes by up to 50 %. The analysis of the quantum efficiency parameter reveals that the most active co-doping In4Co5Nb material utilizes light efficiently. The significant enhancement of catalytic activity under dual excitation demonstrates the potential viability for intensifying thermal (classical) catalytic processes.

Data availability

The data of this article have been included in this published article and its ESI† file. Further information and data will be made available on request.

Author contributions

Luis José Jiménez-Chavarriga, Data curation; Formal analysis; Validation; Visualization; Writing - original draft. Rocío Sayago-Carro, Data curation; Formal analysis; Validation; Visualization; Writing - original draft. Uriel Caudillo-Flores, Data curation; Formal analysis; Funding acquisition; Investigation; Methodology; Project administration; Resources; Validation; Visualization; Writing - review & editing. Irene-Barba Nieto, Data curation; Formal analysis; Validation; Visualization; Writing -

View Article Online
DOI: 10.1039/D5TA08707D

review & editing. Álvaro Tolosana-Moranchel, Data curation; Formal analysis; Validation; Visualization; Writing - review & editing. Jose A. Rodríguez, Investigation; Methodology; Project administration; Resources; Validation; Visualization; Writing - review & editing. Marcos Fernández-García, Conceptualization; Data curation; Formal analysis; Funding acquisition; Investigation; Methodology; Project administration; Resources; Software; Supervision; Validation; Visualization; Writing - original draft; Writing - review & editing. Anna Kubacka, Conceptualization; Data curation; Formal analysis; Funding acquisition; Investigation; Methodology; Project administration; Resources; Software; Supervision; Validation; Visualization; Writing - original draft; Writing - review & editing.

Conflict of interest

The authors declare no conflict of interest.

Acknowledgments

Financial support for this work was obtained through the IN116424 and IV100124 PAPIIT-UNAM (Mexico) projects and through grants PID2022-136883OB-C21 and PCI2024-155031-2 funded by MCIN/AEI/10.13039/501100011033 and, when appropriate, by the "European Union" EU/PRTR and FEDER/EU programs. A. Tolosana-Moranchel thanks the Consejería de Educación, Juventud y Deporte of the Comunidad de Madrid for the Ayuda Destinada a la Atracción de Talento Investigador "César Nombela" (2023-T1/ECO-29095). Dr. D.A. Dominguez, MC. P. Casillas, R. Medoza and J. Romero are acknowledged for the XPS spectra and TEM images, respectively. I.B.-N. thanks, Brookhaven National Laboratory, for funding through the

View Article Online
DOI: 10.1039/D5TA08707D

Goldhaber Distinguished Fellowship program. M.F.G. is fully indebted to Prof. F. Fernández-Martín for its support and guidance.

References

1 S. Shah, S. Hussain, S. T. U. Din, A. Shahid, J. N. O. Amu-Darko, M. Wang, Y. Tianyan, G. Liu and G. Qiao, *J. Environ. Chem. Eng.*, 2024, **12**, 112538.

2 H. Khan, S. Sarkar, M. Pal, S. Bera and S. Jana, in *Post-Transition Metals*, IntechOpen, 2021.

3 A. Kubacka, M. Fernández-García and G. Colón, *Chem. Rev.*, 2012, **112**, 1555–1614.

4 Z. Xiao, P. Li, H. Zhang, S. Zhang, X. Tan, F. Ye, J. Gu, J. Zou and D. Wang, *Fuel*, 2024, **362**, 130906.

5 M. Fernández-García, A. Martínez-Arias, J. C. Hanson and J. A. Rodriguez, *Chem. Rev.*, 2004, **104**, 4063–4104.

6 F. E. Osterloh, *Chem. Soc. Rev.*, 2013, **42**, 2294–2320.

7 I. G. Nielsen, S. Sommer and B. B. Iversen, *Nanoscale*, 2021, **13**, 4038–4050.

8 J. M. Kim, J. K. Park, K. N. Kim, C. H. Kim and H. G. Jang, *Curr. Appl. Phys.*, 2006, **6**, e198–e201.

9 M. M. Cohen, *Introduction to the Quantum Theory of Semiconductors*, 1998.

10 S. T. Bromley, I. de P. R. Moreira, K. M. Neyman and F. Illas, *Chem. Soc. Rev.*, 2009, **38**, 2657.

11 S. P. Harvey, T. O. Mason, D. B. Buchholz, R. P. H. Chang, C. Körber and A. Klein, *J. Am. Ceram. Soc.*, 2008, **91**, 467–472.

12 A. Álvarez, A. Bansode, A. Urakawa, A. V. Bavykina, T. A. Wezendonk, M. Makkee, J. Gascon and F. Kapteijn, *Chem. Rev.*, 2017, **117**, 9804–9838.

13 J. Yan, C. Wang, H. Ma, Y. Li, Y. Liu, N. Suzuki, C. Terashima, A. Fujishima and X. Zhang, *Appl. Catal. B Environ.*, 2020, **268**, 118401.

14 M. Ghoussoub, M. Xia, P. N. Duchesne, D. Segal and G. Ozin, *Energy Environ. Sci.*, 2019, **12**, 1122–1142.

15 V. Nair, M. J. Muñoz-Batista, M. Fernández-García, R. Luque and J. C. Colmenares, *ChemSusChem*, 2019, **12**, 2098–2116.

16 R. Fiorenza, M. Bellardita, S. A. Balsamo, L. Spitaleri, A. Gulino, M. Condorelli, L. D'Urso, S. Scirè and L. Palmisano, *Chem. Eng. J.*, 2022, **428**, 131249.

17 R. Sayago-Carro, I. Barba-Nieto, N. Gómez-Cerezo, J. A. Rodriguez, M. Fernández-García and A. Kubacka, *ACS Appl. Mater. Interfaces*, 2024, **16**, 62131–62141.

18 M. Voccia, S. Kapse, R. Sayago-Carro, N. Gómez-Cerezo, M. Fernández-García, A. Kubacka, F. Viñes and F. Illas, *ACS Appl. Mater. Interfaces*, 2024, **16**, 30157–30165.

19 X. Deng, J. Zhang, K. Qi, G. Liang, F. Xu and J. Yu, *Nat. Commun.*, 2024, **15**, 4807.

20 D. Leshchev, M. Rakitin, B. Luvizotto, R. Kadyrov, B. Ravel, K. Attenkofer and

E. Stavitski, *J. Synchrotron Radiat.*, 2022, **29**, 1095–1106.

21 B. Ravel and M. Newville, *J. Synchrotron Radiat.*, 2005, **12**, 537–541.

22 P. A. Lee, P. H. Citrin, P. Eisenberger and B. M. Kincaid, *Rev. Mod. Phys.*, 1981, **53**, 769–806.

23 C. T. Chantler, F. Boscherini and B. Bunker, Eds., *International Tables for Crystallography. Vol I: X-Ray Absorption Techniques and Related Techniques*, International Union of Crystallography, Chester, England, 2020, vol. I.

24 A. Kubacka, U. Caudillo-Flores, I. Barba-Nieto, M. J. Muñoz-Batista and M. Fernández-García, *Curr. Opin. Colloid Interface Sci.*, 2020, **49**, 42–59.

25 M. Thommes, K. Kaneko, A. V. Neimark, J. P. Olivier, F. Rodriguez-Reinoso, J. Rouquerol and K. S. W. Sing, *Pure Appl. Chem.*, 2015, **87**, 1051–1069.

26 S. Avivi, Y. Mastai and A. Gedanken, *Chem. Mater.*, 2000, **12**, 1229–1233.

27 X. Chang, J. Liu, Z. Guo, Y. Cheng, Q. Yan and Y.-Y. Li, *Appl. Catal. B Environ. Energy*, 2024, **349**, 123858.

28 J. Liqiang, Q. Yichun, W. Baiqi, L. Shudan, J. Baojiang, Y. Libin, F. Wei, F. Honggang and S. Jiazhong, *Sol. Energy Mater. Sol. Cells*, 2006, **90**, 1773–1787.

29 J. D. Henderson, L. Pearson, H. Nie and M. C. Biesinger, *Surf. Interface Anal.*, 2025, **57**, 81–97.

30 J. A. Van Bokhoven and C. Lamberti, Eds., *X-Ray Absorption and X-Ray Emission Spectroscopy*, Wiley, 2016.

31 P. E. Moulder, J. F.; Stickle, W. F.; Sobol, *Handbook of X-ray Photoelectron Spectroscopy: A Reference Book of Standard Data for Use in X-ray Photoelectron Spectroscopy*, Perkin-Elmer, 1993.

32 Z.-P. Hu, G. Qin, J. Han, W. Zhang, N. Wang, Y. Zheng, Q. Jiang, T. Ji, Z.-Y. Yuan, J. Xiao, Y. Wei and Z. Liu, *J. Am. Chem. Soc.*, 2022, **144**, 12127–12137.

33 H. Dau, P. Liebisch and M. Haumann, *Anal. Bioanal. Chem.*, 2003, **376**, 562–583.

34 P. C. Piilonen, F. Farges, R. L. Linnen and G. E. B. Jr., *Phys. Scr.*, 2005, 405.

35 M. A. Sahiner, A. Nabizadeh, D. Rivella, L. Cerqueira, J. Hachlica, R. Morea, J. Gonzalo and J. C. Woicik, *J. Phys. Conf. Ser.*, 2016, **712**, 012103.

36 S. Yan, W. Qiao, W. Zhong, C.-T. Au and Y. Dou, *Appl. Phys. Lett.*, 2014, **104**, 062404.

37 R. D. Shannon, *Acta Crystallogr. Sect. A*, 1976, **32**, 751–767.

38 Y. Xu and M. A. A. Schoonen, *Am. Mineral.*, 2000, **85**, 543–556.

39 N. Katada and M. Niwa, *Catal. Surv. from Asia*, 2004, **8**, 161–170.

40 M. Hu, Z. Yao and X. Wang, *AIMS Mater. Sci.*, 2017, **4**, 755–788.

41 A. Wesner, P. Kampe, N. Herrmann, S. Eller, C. Ruhmlieb and J. Albert, *ChemCatChem*, 2023, **15**, e202301125.

42 Z. Wang, H. Song, H. Liu and J. Ye, *Angew. Chemie Int. Ed.*, 2020, **59**, 8016–8035.

43 N. T. Nguyen, M. Xia, P. N. Duchesne, L. Wang, C. Mao, F. M. Ali, T. Yan, P. Li, Z.-H. Lu and G. A. Ozin, *Nano Lett.*, 2021, **21**, 1311–1319.

44 A. Mena-Saucedo, U. Caudillo-Flores, A. Kubacka and M. Fernández-García, *J. Phys. Chem. C*, 2024, **128**, 20923–20932.

45 L. He, T. E. Wood, B. Wu, Y. Dong, L. B. Hoch, L. M. Reyes, D. Wang, C. Kübel, C. Qian, J. Jia, K. Liao, P. G. O'Brien, A. Sandhel, J. Y. Y. Loh, P. Szymanski, N. P. Kherani, T. C. Sum, C. A. Mims and G. A. Ozin, *ACS Nano*, 2016, **10**, 5578–5586.

46 A. Mohan, U. Ulmer, L. Hurtado, J. Loh, Y. F. Li, A. A. Tountas, C. Krevert, C. Chan, Y. Liang, P. Brodersen, M. M. Sain and G. A. Ozin, *ACS Appl. Mater. Interfaces*, 2020, **12**, 33613–33620.

47 K. I. Hadjiivanov, D. A. Panayotov, M. Y. Mihaylov, E. Z. Ivanova, K. K. Chakarova, S. M. Andonova and N. L. Drenchev, *Chem. Rev.*, 2021, **121**, 1286–1424.

View Article Online
DOI: 10.1039/D5TA08707D

Tables and Figures

Table 1. Main physico-chemical properties of the solids.

Catalyst	BET area (m^2 g^{-1})	Pore volume (cm^3 g^{-1})	Particle size (nm)[a]	Band gap (eV)
In_2O_3	146 ± 9	0.46 ± 0.04	$6.1 \pm 0.5_5$	2.70 ± 0.11
In5Nb	121 ±7	0.39 ± 0.03	6.8 ± 0.6	2.80 ± 0.08
In4Co	116 ± 7	0.37 ± 0.03	7.7 ± 0.7	3.20 ± 0.10
In4Co2.5Nb	88 ± 5	0.11 ± 0.01	7.6 ± 0.7	3.10 ± 0.10
In4Co5Nb	84 ± 5	0.34 ± 0.03	$7.2 \pm 0.6_5$	3.00 ± 0.09
In4Co7.5Nb	$74 \pm 4._5$	0.43 ± 0.03	10.0± 0.9	3.00 ± 0.10

a) Measured for the bixbyite-type In_2O_3 structure.

View Article Online
DOI: 10.1039/D5TA08707D

Table 2. Co K-edge EXAFS fitting results for the samples. Samples are presented by their names, followed by k and R ranges of fitting.

Shell	R (Å)	N	$\Delta\sigma^2$ (10^2 Å^2)	E_0 (eV)
In4Co: 3.20-11.00 Å^{-1}; 1.00-3.95 Å				
Co-O	2.00±0.01	5.6±0.6	1.5±0.1	-4.5±0.5
Co-In	3.30±0.01	4.2±0.4	0.9±0.1	-4.5±0.5
Co-In	3.80±0.02	5.6±0.6	1.8±0.2	-4.5±0.5
Co-Co	3.20±0.02	0.5±0.05	0.4±0.05	-4.5±0.5
In4Co2.5Nb: 3.20-10.70Å^{-1}; 1.00-3.95 Å Å				
Co-O	2.10±0.01	6.0±0.6	1.4±0.2	-4.1±0.4
Co-In	3.30±0.01	3.2±0.3	0.9±0.1	-4.1±0.4
Co-In	3.80±0.01	5.9±0.6	1.9±0.2	-4.1±0.4
Co-Co	3.20±0.05	0.2±0.03	0.4±0.06	-4.1±0.4
In4Co5Nb; 3.20-10.50 Å^{-1}; 1.00-3.95 Å				
Co-O	2.00±0.01	5.7±0.6	1.5±0.1	-4.2±0.3$_5$
Co-In	3.30±0.01	3.9±0.4	0.9±0.1	-4.2±0.3$_5$
Co-In	3.80±0.02	5.9±0.6	1.8±0.2	-4.2±0.3$_5$
Co-Co	3.20±0.02	0.5±0.05	0.4±0.05	-4.2±0.3$_5$
In4Co7.5Nb: 3.20-10.50 Å^{-1}; 1.00-3.95Å				
Co-O	2.00±0.01	6.1±0.6	1.6±0.3	-4.9±0.4
Co-In	3.30±0.02	3.2±0.3	0.9±0.1	-4.9±0.4
Co-In	3.80±0.02	5.6±0.6	1.8±0.2	-4.9±0.4
Co-Co	3.20±0.03	0.3±0.06	0.3±0.06	-4.9±0.4

Table 3. Nb K-edge EXAFS fitting results for the samples. Samples are presented by their names, followed by k and R ranges of fitting.

Shell	R (Å)	N	$\Delta\sigma^2$ (10^3 Å^2)	E_0 (eV)
In5Nb: 3.00-11.00 Å^{-1}; 1.10-3.95 Å				
Nb-O	1.90± 0.01	2.4± 0.2	6.0±0.8	0.2±0.1
Nb-O	2.10±0.01	2.0±0.2	6.0±0.4	0.2±0.1
Nb-In	3.40±0.01	6.0±0.6	8.5±1.3	0.2±0.1
In4Co2.5Nb: 3.00-11.00 Å^{-1}; 1.15-3.95 Å				
Nb-O	2.00±0.01	3.3±0.3	2.0±0.6	7.6±0.5
Nb-O	2.10±0.02	2.9±0.3	2.0±0.9$_5$	7.6±0.5
Nb-In	3.40±0.01	5.4±0.5	8.3±0.8	7.6±0.5
In4Co5Nb; 3.00-10.50 Å^{-1}; 1.10-3.95 Å				
Nb-O	1.98±0.01	3.4±0.3	2.9±0.2	7.4±0.6
Nb-O	2.07±0.02	2.4$_5$±0.2	1.0±0.3	7.4±0.6
Nb-In	3.38±0.01	6.1±0.61	8.6±0.8	7.4±0.6
In4Co7.5Nb: 3.00-10.50 Å^{-1}; 1.15-3.95 Å				
Nb-O	1.93±0.01	2.7±0.3	2.9±0.1	7.4±0.5
Nb-O	2.01±0.02	2.9±0.3	3.0±0.5	7.4±0.5
Nb-In	3.38±0.02	4.6±0.5	8.2±0.8	7.4±0.5

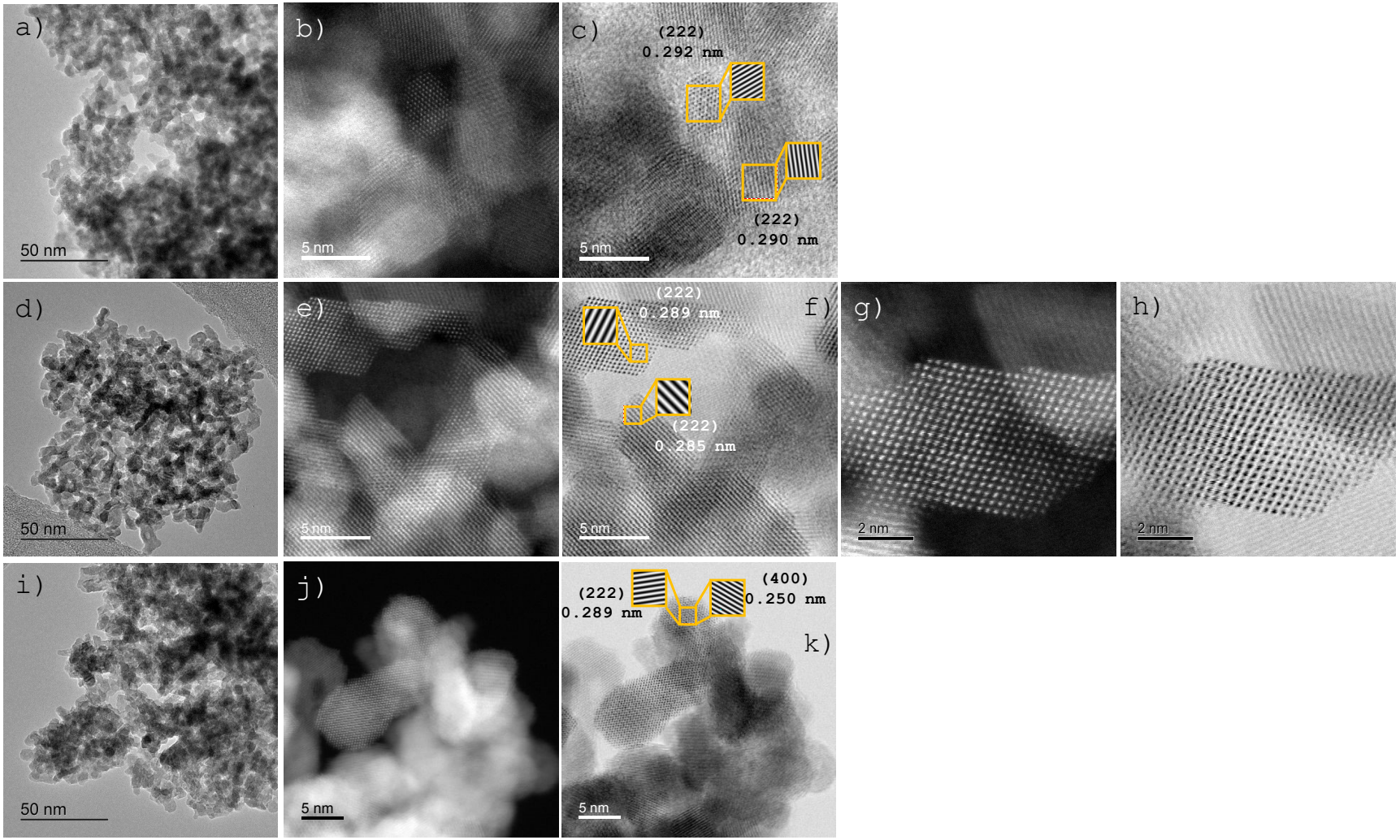

Figure 1. Bright and Dark HR-TEM micrographs for the In4Co (a-c), In4Co5Nb(d-h), and In5Nb (i-k) samples.

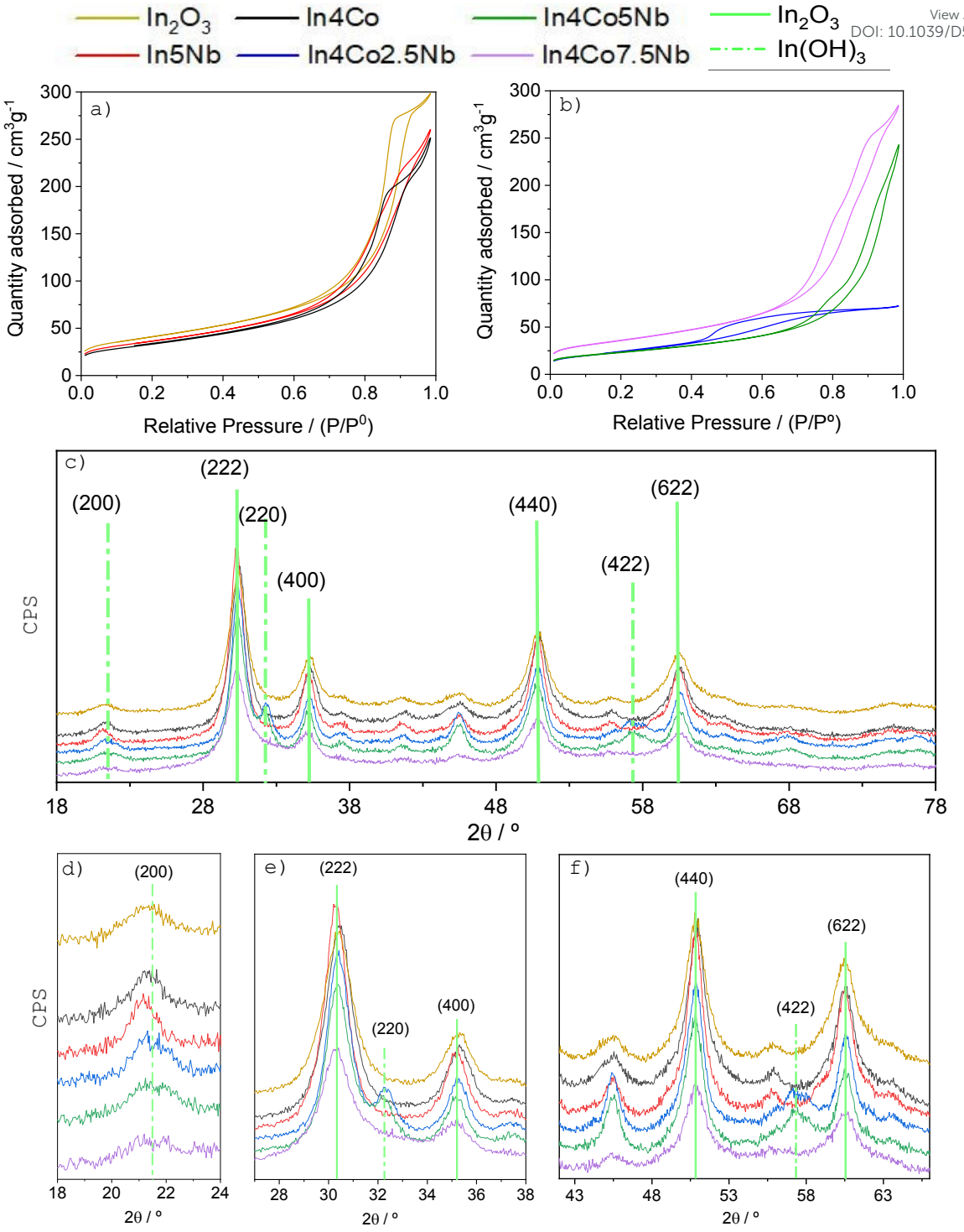

Figure 2. (a,b) Nitrogen adsorption-desorption isotherms for the samples; (c) XRD patterns for the samples; (d-f) zoom views for specific angles of panel c. In panels c-f main peaks of the bixbyite In_2O_3 (fill) and $In(OH)_3$ (dashed-dot) structures are marked with green lines. See text for details.

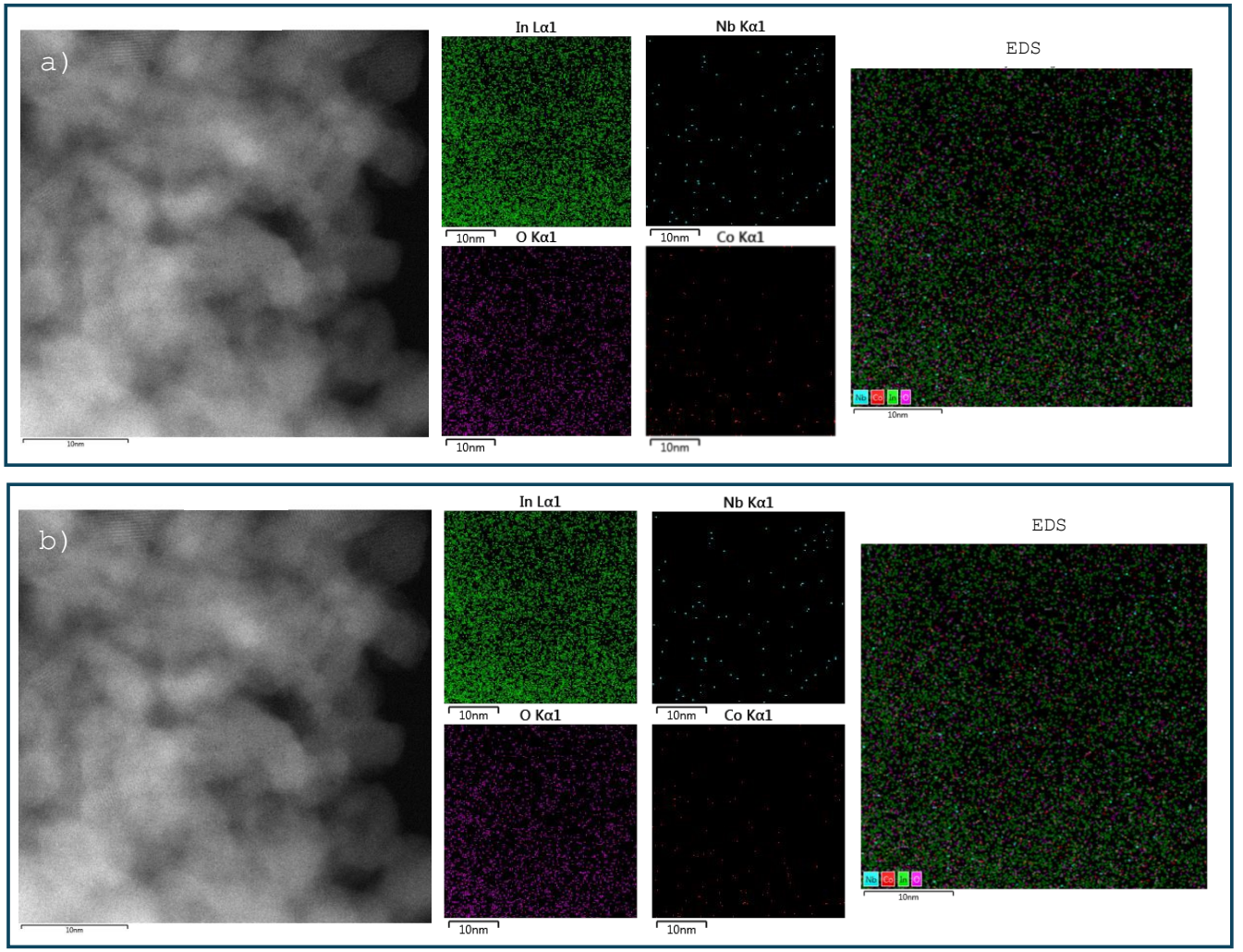

Figure 3. Dark-field HR-TEM micrographs and EDS analysis of the In4Co2.5Nb (a) and In4Co7.5Nb (b) samples.

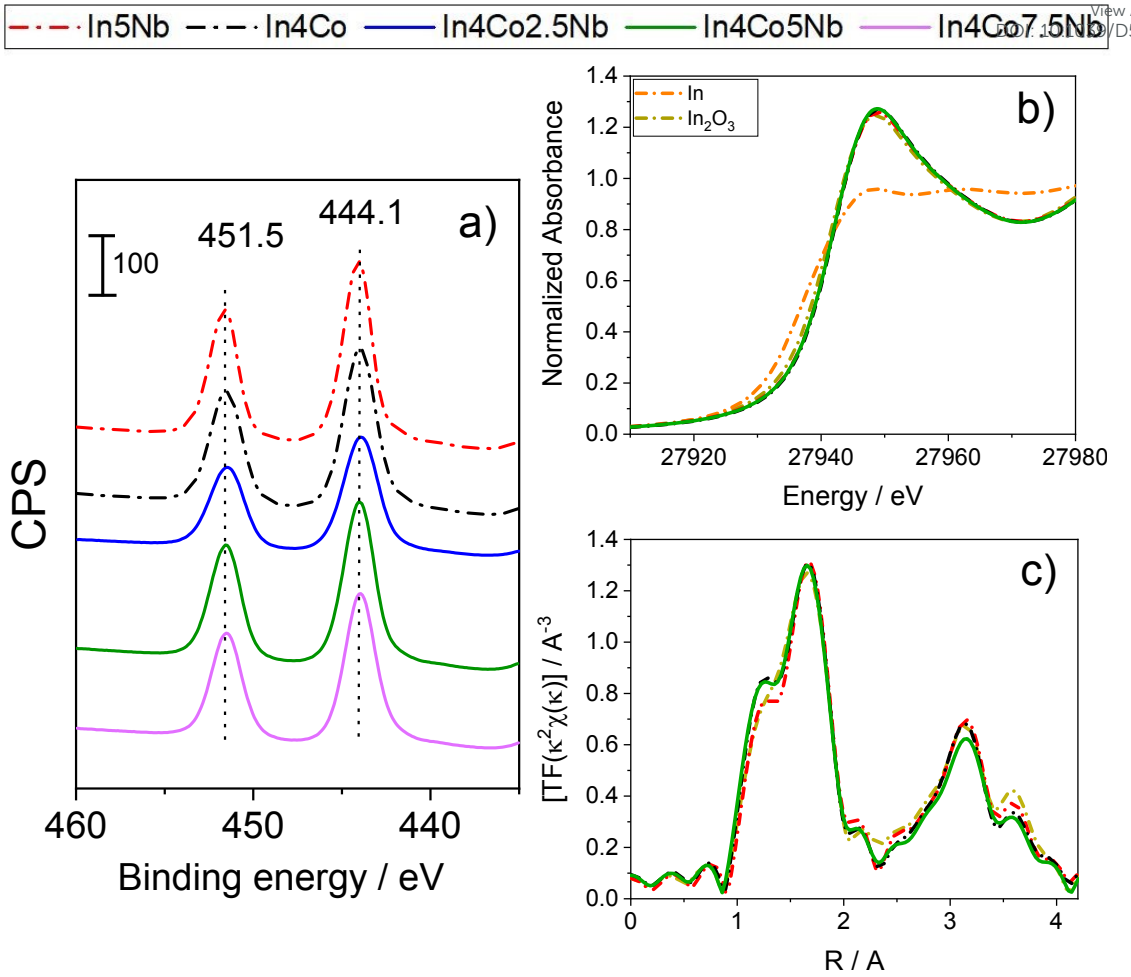

Figure 4. (a) In 3d XPS spectra for the samples; (b) In K-edge XANES spectra for the samples and references; and (c) K^2-weighted Fourier transform of the In K-edge EXAFS spectra for the samples and references. See text for details.

View Article Online
DOI: 10.1039/D5TA08707D

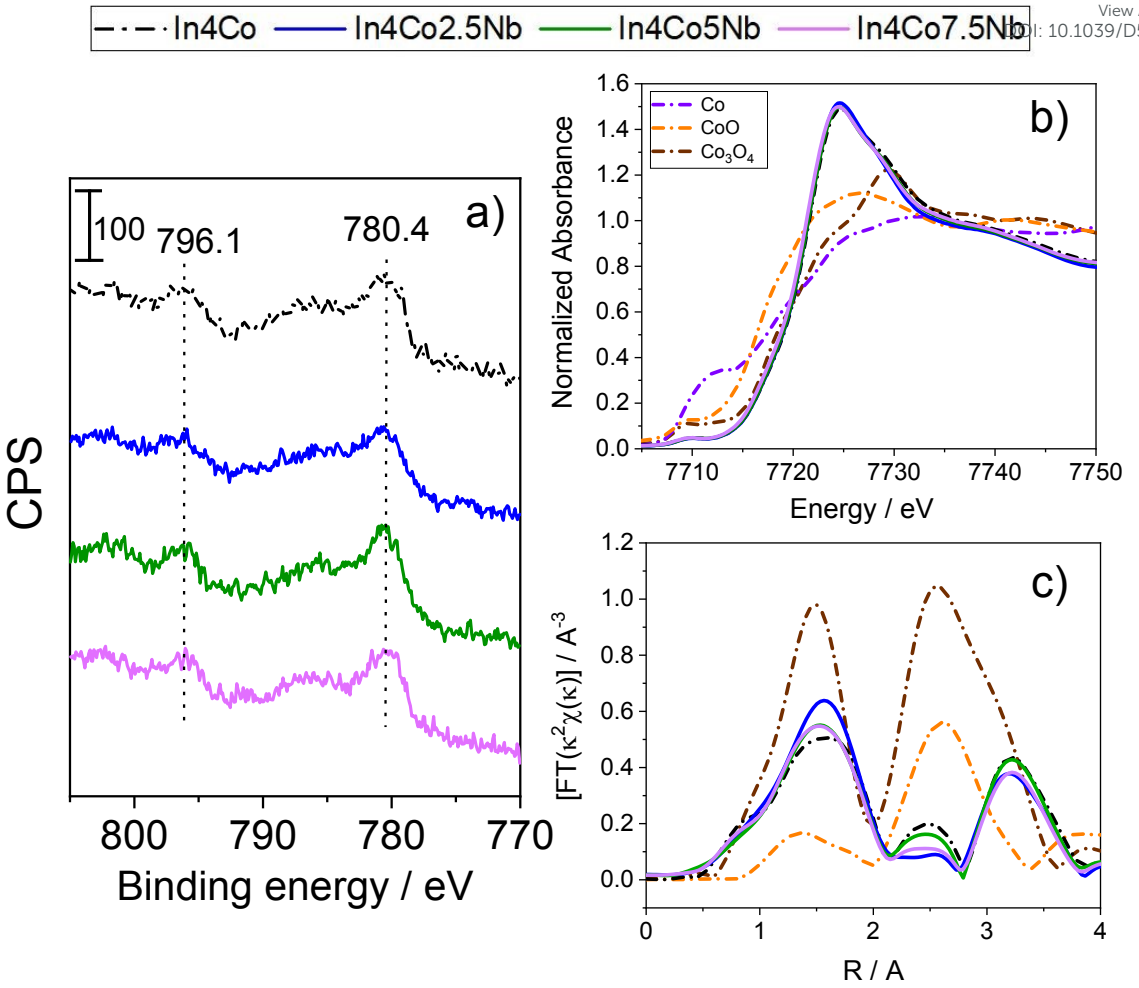

Figure 5. (a) Co 2pXPS spectra for the samples; (b) Co K-edge XANES spectra for the samples and references; and (c) K^2-weighted Fourier transform of the Co K-edge EXAFS spectra for the samples and references. See text for details.

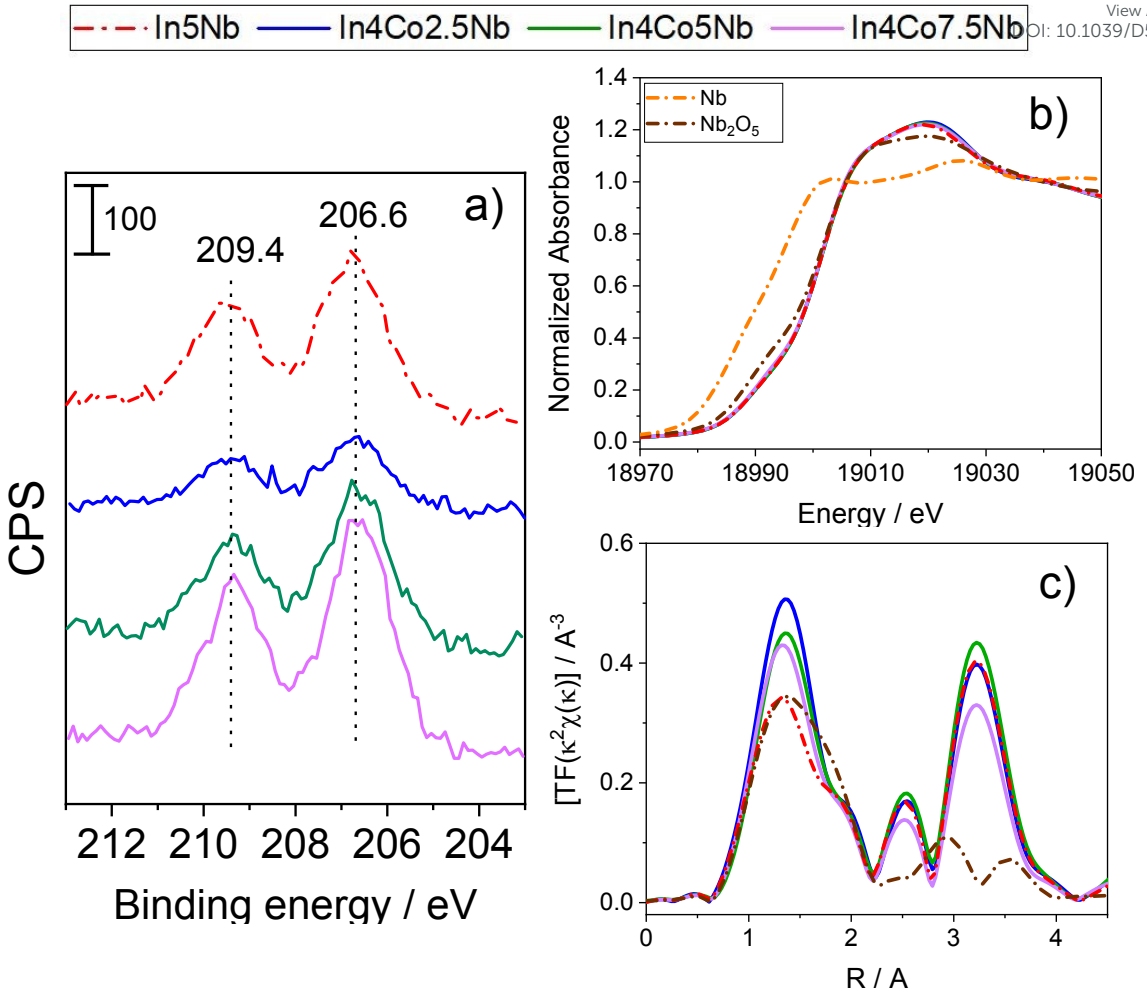

Figure 6. (a) Nb 3d XPS spectra for the samples; (b) Nb K-edge XANES spectra for the samples and references; and (c) K^2-weighted Fourier transform of the Nb K-edge EXAFS spectra for the samples and references. See text for details.

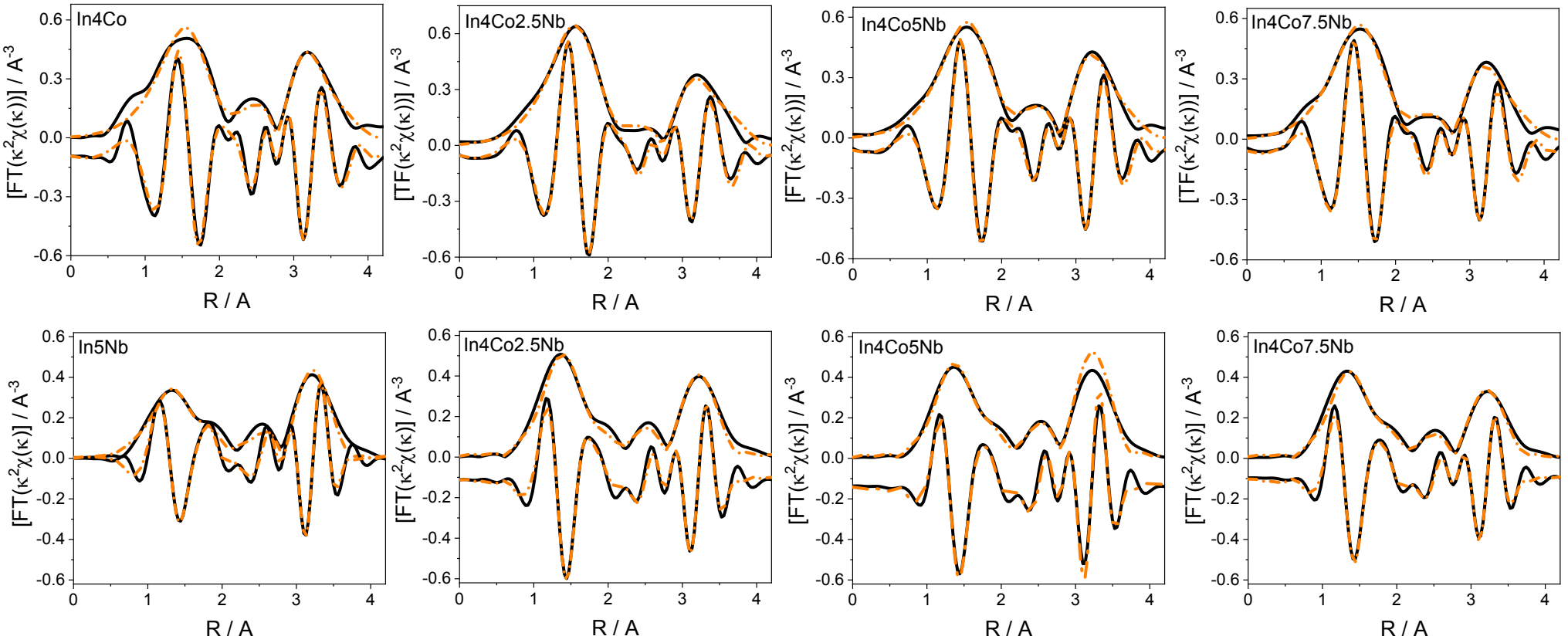

Figure 7. K^2-weighted Fourier transform of the EXAFS signal and fitting results. Black full/dashed lines display the experimental signals for the module and the imaginary part of the Fourier transform. Orange full/dashed lines display the fitting results for the module and the imaginary part of the Fourier transform. Upper row: Co K-edge. Lower row: Nb K-edge.

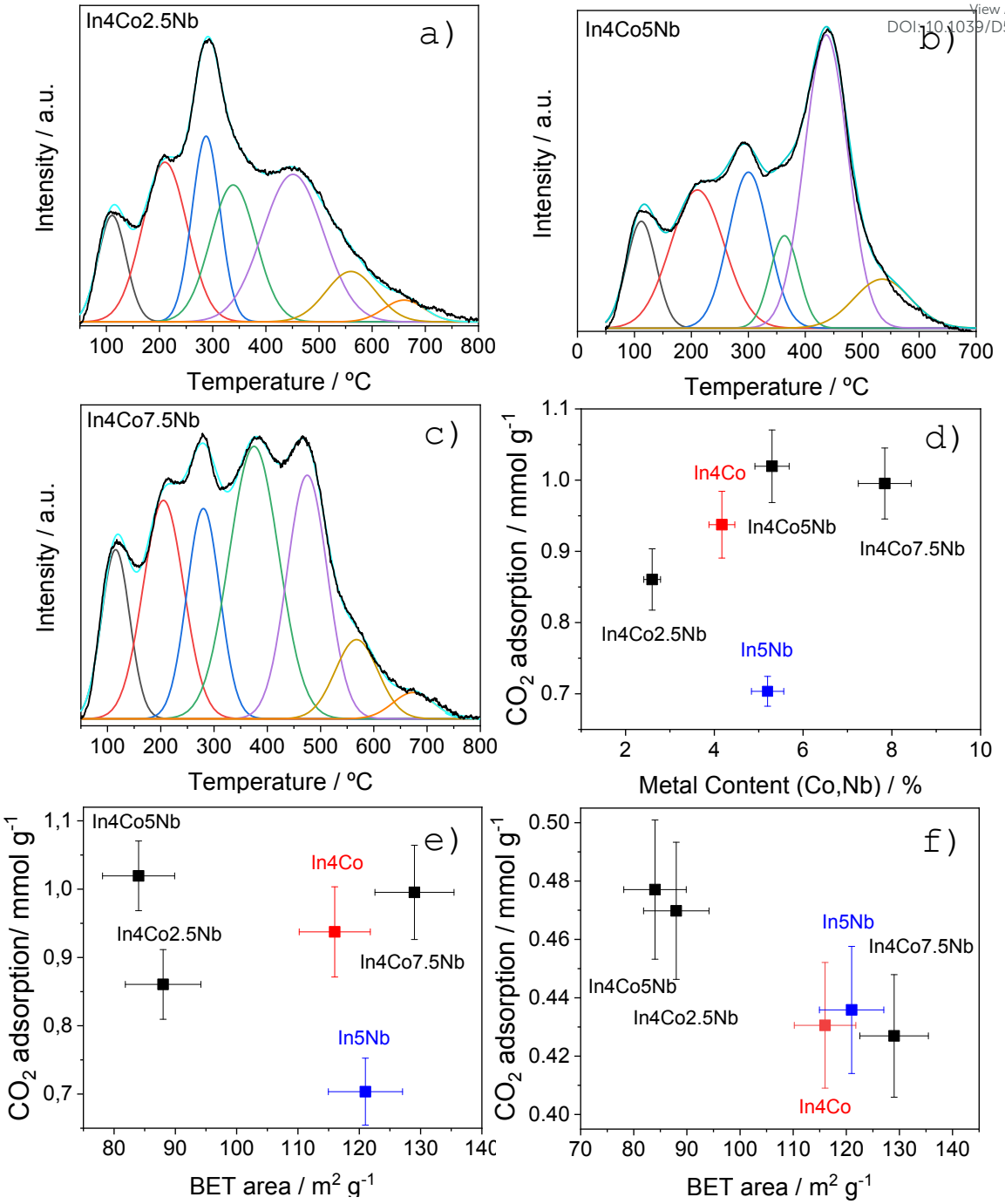

Figure 8. TPD results; (a-c) experimental and fitting results for co-doped solids; (d) amount of CO_2 adsorption as a function of the doping content of the samples; (e) amount of CO_2 adsorption as a function of the BET area of the samples; and (f) amount of CO_2 desorbed in the 100-350 ºC temperature range as a function of the BET area of the samples. See text for details.

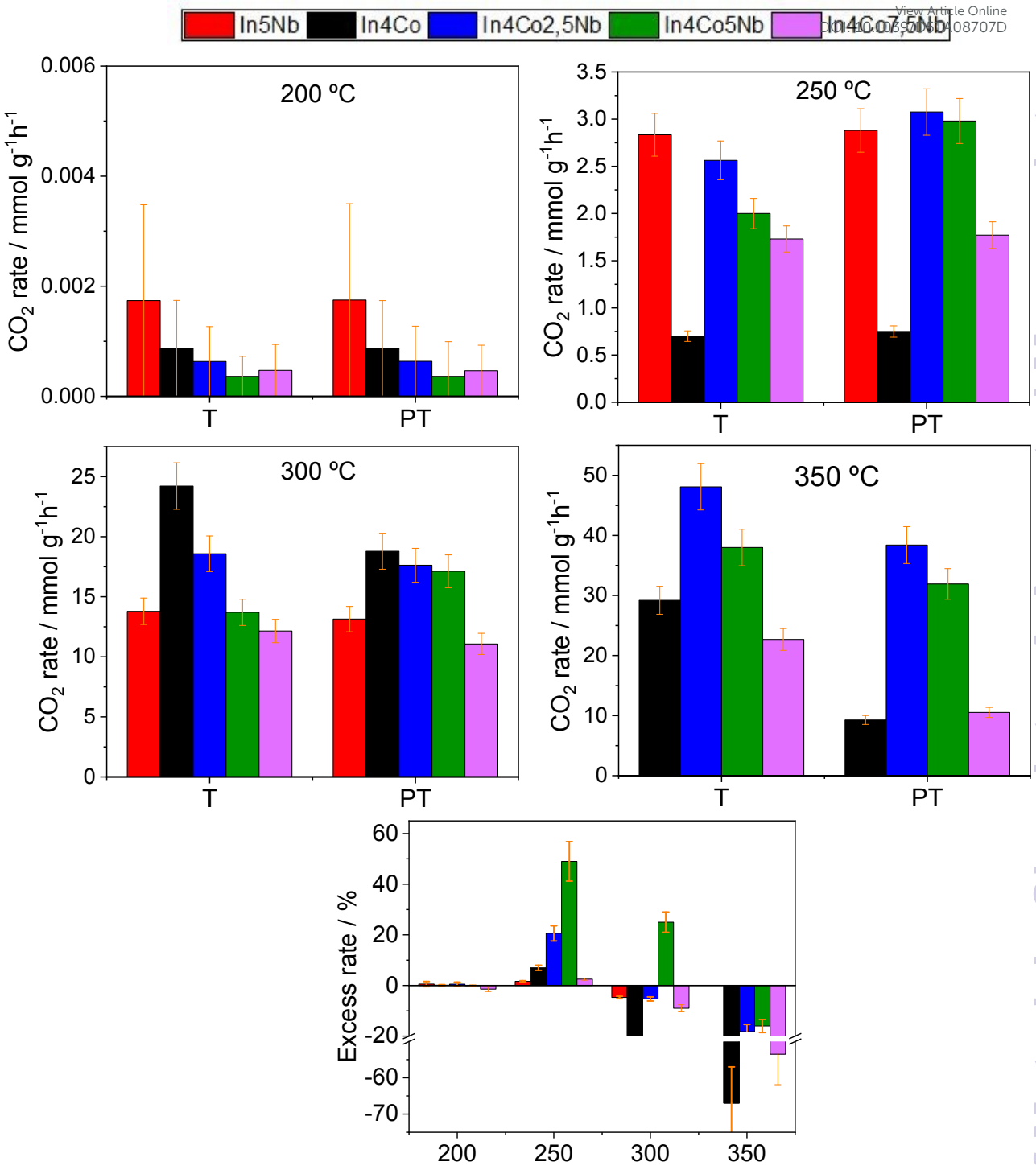

Figure 9. Thermal (T) and photothermal (PT) reaction rates obtained at different reaction temperatures for the samples. Bottom panel displays the excess reaction rates as measured in equation S1. See text for details.

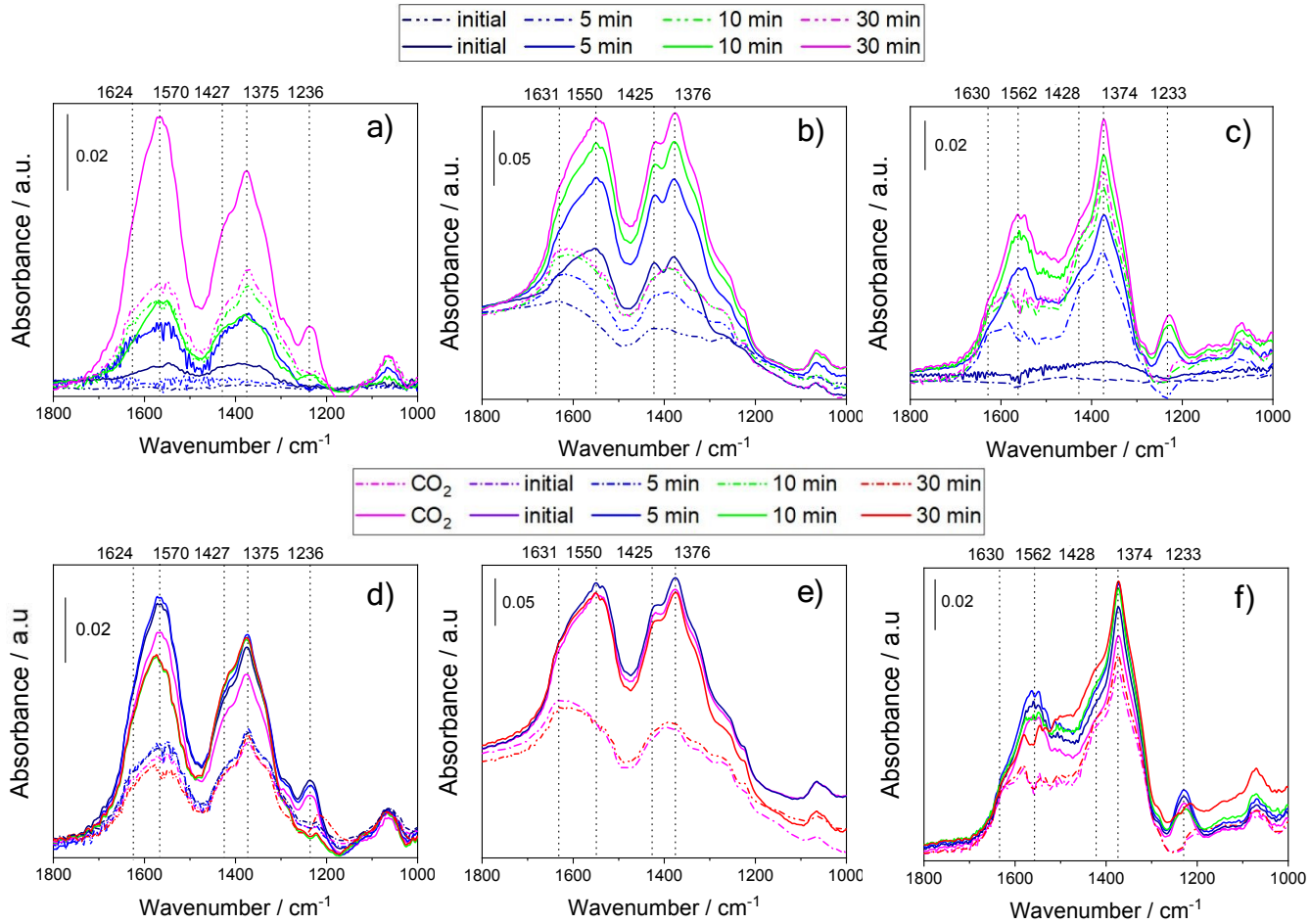

Fig. 10. In-situ infrared spectra of the samples subjected to consecutive 20 % CO_2/N_2 (upper row) and 20 % H_2/N_2 (lower row) streams at 250 ℃. (a,d) In4Co5Nb; (b,e) In5Nb; and (c,f) In4Co sample. Dashed line; thermal experiment; Full lines; photothermal experiment. See text for details.

View Article Online
DOI: 10.1039/D5TA08707D

Data availability statement

The data of this article have been included in this published article and its ESI† file. Further information and data will be made available on request.